Original Paper

Effect of proppant pumping schedule on the proppant placement for supercritical CO$_2$ fracturing

Yong Zheng [a], Hai-Zhu Wang [a, *], Ying-Jie Li [b], Gang-Hua Tian [a], Bing Yang [a], Cheng-Ming Zhao [a], Ming-Sheng Liu [a]

[a] State Key Laboratory of Petroleum Resources and Prospecting, China University of Petroleum (Beijing), Beijing, 102249, China
[b] CNPC Offshore Engineering Co. Ltd., Beijing, 100028, China

A B S T R A C T

Supercritical CO$_2$ fracturing is a potential waterless fracturing technique which shows great merits in eliminating reservoir damage, improving shale gas recovery and storing CO$_2$ underground. Deep insight into the proppant-transport behavior of CO$_2$ is required to better apply this technique in the engineering field. In the present paper, we adopted a coupled Computational Fluid Dynamics and Discrete Element Method (CFD-DEM) approach to simulate the proppant transport in a fracking fracture with multiple perforation tunnels. Previous experiments were first simulated to benchmark the CFD-EDM approach, and then various pumping schedules and injection parameters (injection location, multi-concentration injection order, multi-density injection order and injection temperature) were investigated to determine the placement characteristics of proppant. Results indicate that the swirling vortex below the injection tunnels dominates the proppant diffusion in the fracture. The velocity of fluid flow across the proppant bank surface in multi-concentration injection shows a positive correlation with the proppant concentration. Injecting high-density proppant first can promote the transportation of low-density proppant injected later in the fracture to a certain extent. Decreasing the initial injection temperature of supercritical CO$_2$ slurry helps enhance the particle-driving effect of fluid and improve the performance of supercritical CO$_2$ in carrying proppant.
© 2021 The Authors. Publishing services by Elsevier B.V. on behalf of KeAi Communications Co. Ltd. This is an open access article under the CC BY-NC-ND license (http://creativecommons.org/licenses/by-nc-nd/4.0/).

1. Introduction

Over the past few decades, as a result of rapid economic development, industrialization and urbanization, global CO$_2$ emissions have continued to increase, and the environmental challenges posed by rising levels of CO$_2$ in the atmosphere have become a matter of growing public concern. It is generally accepted that a reduction of the CO$_2$ emissions is an effective way to promote climate change. Hence, many CO$_2$ reduction technologies and methods have been proposed worldwide, among which carbon capture and storage (CCS) is one of the important strategies (Holloway, 2005; Leung et al., 2014). However, due to concerns about the high cost of CCS, carbon capture utilization and storage (CCUS) technology has been developed, which enables resource utilization while storing CO$_2$ (Cuéllar-Franca and Azapagic, 2015; Li

et al., 2013; Norhasyima and Mahlia, 2018), making it a strong prospect.

Among various utilization ways of CO$_2$, the application in oil and natural gas industry is a crucial component (Norhasyima and Mahlia, 2018). Enhancing oil recovery by injecting CO$_2$ into depleted reservoirs (CO$_2$-EOR) is a well-known practice in oil and natural gas industry and has developed into a mature technology (Alvarado and Manrique, 2010). CO$_2$-EOR technology is likely to be suitable for more than 90% of the world's estimated ultimately recoverable oil (Godec, 2011), and it is also considered an option for permanent CO$_2$ storage (Dai et al., 2014). Thus, the use of CO$_2$-EOR has the dual advantages of reducing CO$_2$ emissions and increasing oil production. Furthermore, CO$_2$ also plays an important role in the extraction of unconventional natural gas such as shale gas (Iddphonce et al., 2020). The application of hydraulic fracturing has led to a boom in shale gas production over the past few years, yet the significant environmental controversy it faces has prompted the industry and researchers to explore waterless fracturing fluids

to reduce water use (Clark et al., 2013; Middleton et al., 2017; Vengosh et al., 2014). The potential effectiveness and unique advantages of CO_2 make it one of the most interested waterless fracturing fluids.

Similar to hydraulic fracturing, liquid or supercritical CO_2 is injected at high pressure into the shale formation at a flow that exceeds the absorption capacity of the formation to open the existing fractures or initiate new fractures, thereby increasing conductivity of the shale formation. Under the temperature-pressure conditions of shale reservoirs, CO_2 can easily reach the supercritical state (pressure over 7.38 MPa, temperature over 304.1 K). Compared with water-based fracturing fluids, supercritical CO_2 as a working fluid has several significant advantages. Firstly, supercritical CO_2 fracturing is inclined to form a complex network of fractures in the reservoir due to its low viscosity, and enhance the reservoir stimulation effect (Chen et al., 2021b; Li et al., 2018; Song et al., 2019; Yang et al., 2021). At the same time, there is no water in the fluid, which will not cause water block and swelling of clay minerals that can impair the hydrocarbon migration pathway (Bahrami et al., 2012; Dehghanpour et al., 2012; Middleton et al., 2015; Naik et al., 2019). Moreover, CO_2 has an obvious tendency to adsorb to shale compared to methane (Hamza et al., 2021; Huo et al., 2017; Wang et al., 2021), which means that it can replace the methane adsorbed in shale and achieve permanent storage of CO_2 while increasing shale gas production and recovery. Based on these potential advantages, supercritical CO_2 fracturing is considered to be a waterless fracturing technology with strong growth prospects (Chen et al., 2021a; Middleton et al., 2015; Mojid et al., 2021; Wang et al., 2012, 2019).

In addition, fracturing the reservoir will require the pumping of supercritical CO_2 slurry, a mixture of supercritical CO_2 fluid and proppant particles, into the fracture, which will determine the future production performance of the well (Rightmire et al., 2005). A proppant is a solid particle used to support fractures created by fracturing to prevent them from closing again after the operation is completed. It works by forming a support fracture zone that is much higher than the reservoir permeability, providing a highly conductive channel for the flow of oil and gas from the reservoir to the wellbore. In order to obtain optimal fracture conductivity and to predict the productivity of the fractured well, the transport behavior and placement of proppant in the fracture has been studied extensively (Qu et al., 2021; Roostaei et al., 2020; Sahai and Moghanloo, 2019). However, it is noteworthy that the majority of these existing studies are for conventional fracturing fluids, i.e., gel and slickwater, and relatively little effort has been conducted in the past on the proppant carried by supercritical CO_2.

Carrying the proppant is a major challenge facing supercritical CO_2 fracturing technology currently (Mojid et al., 2021; Wang et al., 2020). The low viscosity characteristic of supercritical CO_2, while favoring the induction of complex fracture networks, also limits its ability to carry proppant and thus largely hinders its widespread application. Although CO_2 fracturing has been tested and explored by the industry for a long time (Gupta and Bobier, 1998), research into its ability to carry proppant for placement has only begun in recent years (Sun et al., 2018; Wang et al., 2018; Wang and Elsworth, 2020; Zheng et al., 2020). What's more, it is surprising that little research has been reported on supercritical CO_2 slurry pumping schedule, and the effect of different pumping schedule on proppant placement is poorly understood.

In the present study, we studied the proppant transport and placement in a planar fracture with perforation tunnel under different pumping schedule using developed CFD-DEM model. Further validation of the model is performed with experimental results. Based on the model, the effects of injection location, multi-concentration injection order, multi-density injection order and injection temperature on the proppant placement are investigated. The results of this study are to provide a better understanding of the proppant placement in supercritical CO_2 fracturing and can assist fracturing engineers solve problems related to proppant pumping design in fracturing.

2. Numerical model

2.1. Mathematics model

A CFD-DEM based multiphase model was established to simulate the flow of supercritical CO_2 slurry. The fluid phase is described by Navier−Stokes equation based on an Eulerian approach in CFD-DEM model. The DEM method is used to track the proppant particles in the system, and Newton's second law is applied to govern its movement. A detailed description of this model can be found in our previous work (Zheng et al., 2020). However, in the previous model, the heat transfer between fluid-matrix is neglected in simulation. In the present study, we further considered the heat transfer between the supercritical CO_2 fluid and the fracture wall. The energy equation for fluid flow and fracture wall are respectively written as:

$$\frac{\partial}{\partial t}(\rho_f E) + \nabla \cdot (\vec{v}_f(\rho_f E + p)) = \nabla \cdot (k_{eff}\nabla T_f + (\bar{\bar{\tau}}_{eff} \cdot \vec{v}_f)) + S_h. \tag{1}$$

$$\frac{\partial}{\partial t}(\rho_s h) = \nabla \cdot (k_s \nabla T_{wall}). \tag{2}$$

$$E = h - \frac{p}{\rho_f} + \frac{v_f^2}{2} \tag{3}$$

where ρ_f, ρ_s are the densities of supercritical CO_2 fluid and solid wall respectively, kg/m³; E is the specific internal energy, J/kg; $\vec{v}_f$ is the velocity of the fluid, m/s; $\bar{\bar{\tau}}$ is stress tensor, N/m²; p is the static pressure, Pa; k_{eff} and k_s represent the thermal conductivities of fluid and solid wall, W/(m·K); T_f and T_{wall} are the fluid and the fracture wall temperatures, respectively, K; S_h refers to the volumetric heat sources; h is the sensible enthalpy, J/kg.

2.2. CO_2 properties

The physical properties of CO_2 fluid are very sensitive to the changes of temperature and pressure, and CO_2 will reach super-critical state under the reservoir temperature and pressure. Therefore, it is important to effectively calculate the physical properties of supercritical CO_2 to study the flow of supercritical CO_2 slurry within the fracture. The parameters of CO_2 properties used in the model include density, viscosity and thermal conductivity. The widely accepted Span-Wagner equation of state (Span and Wagner, 1996) is used to calculate the fluid density, and the equation is adopted and recommended by the National Institute of Standards and Technology (NIST). The viscosity and thermal conductivity of the fluid are calculated using the explicit models developed by Heidaryan et al. (2011) and Jarrahian and Heidaryan (2012) for calculating CO_2 in the supercritical state, respectively. The average absolute relative error (AARE) of the two models are 1.82% and 2.4%, respectively, compared with NIST web book data, and the accuracy can meet the engineering calculation requirements. The use of explicit CO_2 physical property calculation models is more efficient because they do not require a large number of parameters and complex calculations.

The viscosity can be formulated as (Heidaryan et al., 2011) :

$$\mu = \frac{A_1 + A_2 p + A_3 p^2 + A_4 \ln(T) + A_5 (\ln(T))^2 + A_6 (\ln(T))^3}{1 + A_7 p + A_8 \ln(T) + A_9 (\ln(T))^2} \quad (4)$$

where the viscosity is expressed in centipoise (mPa·s); and the temperature and pressure are expressed in K and bar, respectively.

The thermal conductivity can be formulated as (Jarrahian and Heidaryan, 2012) :

$$\lambda = \frac{C_1 + C_2 p + C_3 p^2 + C_4 \ln(T) + C_5 \ln(T)^2}{1 + C_6 p + C_7 \ln(T) + C_8 \ln(T)^2 + C_9 \ln(T)^3} \quad (5)$$

where the temperature and pressure are expressed in K and MPa, respectively; λ is the thermal conductivity, mW/(m·K); A and C are tuned coefficients, the values of which can be found in the corresponding references.

2.3. Model geometry

In reservoir fracturing, it is generally assumed that there are symmetrical plane fractures with two wings. Fracturing operations usually result in irregular and tortuous fractures. However, in previous numerical models of proppant transport, these fractures are usually represented as a vertical planar, which is a widely used and effective simplification (Sahai and Moghanloo, 2019). Therefore, a rectangular channel with perforation tunnel is used to mimic the supercritical CO_2 slurry injection process in the vertical fracture of a perforation completion. Due to the large consumption of computational resources by CFD-DEM method, a small-scale fracture characterization unit is used in this paper to simulate the transport process of proppant within artificial fractures. The fracture geometry is 500 mm in length, 150 mm in height, and 2 mm in width. Four injection points 3 mm high and 2 mm wide are on the left boundary, whose centers are separated by 12 mm, as shown in Fig. 1. On the right side, the fluid can flow out along the height of the fracture, but proppant particles will be left in the fracture. Furthermore, the effects of fracture propagation and fluid leak-off are neglected in the model.

2.4. Simulation conditions

At the inlets, the supercritical CO_2 slurry enters the computational domain with a specified velocity and temperature. The velocity and temperature of the proppant particles at the initial injection are the same as those of the fluid. In a conventional

hydraulic fracturing operation, the average velocity of slurry in the fracture is mostly below 0.25 m/s, and the flow velocity of slurry in such fractures has been discussed by others before (Alotaibi et al., 2019). We choose the higher value, 0.16 m/s, as the average velocity of slurry in the fracture in this simulation. Therefore, for the fractures (150 mm high and 2 mm wide) and perforation clusters (4 perforations of 3 mm high and 2 mm wide) used in our simulation, the fluid velocity in each perforation is approximately 2.0 m/s. In this paper, uniform spheres are used to represent proppant particles. The fluid flows out under constant pressure boundary conditions. The external pressure at the outlet is set at 18 MPa. The proppant concentration used in the simulation is the ratio of proppant particle volume to fluid volume. In order to explore the effect of heat transfer between fluid and fracture wall on proppant placement, the initial temperature of fluid injection is lower than the wall temperature in the simulation, and this setting is also similar to the actual flow situation in operation (Meng et al., 2018). Therefore, the temperature of fracture wall is fixed at 358 K, which is higher than the initial temperature of supercritical CO_2 slurry.

The fluid governing equation is solved by the finite volume method. The Phase Coupled SIMPLE scheme (Patankar, 1980) is used to treat the coupling between pressure and momentum. The momentum, volume fraction and energy equations are discretized by the first order upwind difference scheme. The wall of the fracture model adopts the non-slip fluid boundary condition, that is, assuming that the velocity of the fluid on the fracture wall is zero. The time step for the fluid phase is 1×10^{-3} s while the time step for the solid phase is 1×10^{-5} s. The Young's modulus, restitution coefficient, Poisson's ratio and friction coefficient of the proppant used by Baldini et al. (2018) were used in the simulation. The elastic parameters of the reservoir rock are obtained from the work of Moghadam et al. (2019). The values of some main parameters used in simulations are listed in Table 1.

3. Results and analysis

3.1. Model validation

This CFD-DEM model has been validated in our previous work, which has an efficient performance in simulating the proppant transport behavior within the fracture (Zheng et al., 2020). However, for the sake of completeness, we further compared the proppant bank profiles in the simulation with the experimental results of Tong and Mohanty (2016) on the basis of the previous verification. The length, height and width of the main fracture in the experiment are 381, 76.2, and 2 mm, respectively. The angle
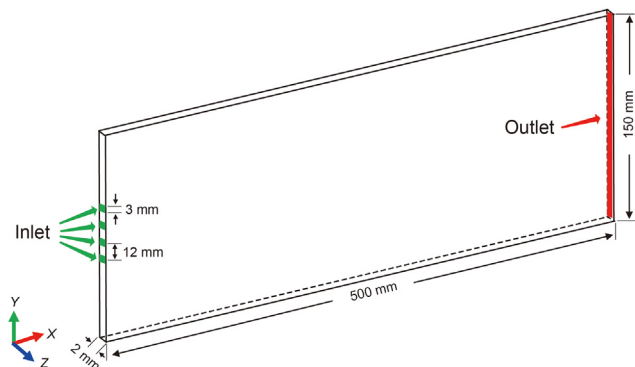

Fig. 1. Sketch of the fracture geometry (not to scale).

Table 1
Numerical parameters.

Parameters	Values
Proppant density ρ_s, kg/m^3	1250, 2650, 3500
Proppant diameter d_s, mm	0.5
Injection temperature T_f, K	328, 338, 348
Wall temperature T_w, K	358
Slurry injection velocity V_{slu}, m/s	2
Particle volumetric concentration C_0	0.02, 0.04, 0.06, 0.08
Outlet pressure P, MPa	18
Particles:	
Young's modulus E_p, Pa	5×10^6
Poisson's ratio v_p	0.5
Wall:	
Young's modulus E_w, Pa	3×10^{10}
Poisson's ratio v_w	0.3
Restitution coefficient e	0.7
Static frication coefficient μ_s	0.5
Rolling friction coefficient μ_r	0.01

Table 2
Parameters used in model validation.

| Parameters	Values
Proppant density ρ_s, kg/m^3	2650
Proppant diameter d_s, mm	0.6
Fluid density ρ_f, kg/m^3	998.2
Fluid viscosity μ_f, mPa·s	1
Slurry injection velocity V_{slu}, m/s	0.1
Particle volumetric concentration C_0	0.038

between the secondary fracture and the main fracture is 90°, the length of the secondary fracture is 190.5 mm, and the height and width are the same as that of the main fracture. The slickwater slurries were injected from the right side of the fracture. The fracture size used in the simulation is the same as that in the laboratory experiment. The basic parameters used in model validation are listed in Table 2.

Fig. 2 shows the profiles of the proppant dune in the main fracture and bypass fracture from numerical results and experimental data under different time moments. It is clear that the proppant distribution obtained from the numerical simulation is in line with the experimental observation. The discrepancy is mainly due to the lack of understanding of the composition and properties of the proppant and fracture wall materials in the experiment, which is needed for CFD-DEM calculation. In addition, the proppant used in the simulation was a sphere of consistent diameter, whereas the experiments used 20/40 mesh sand, which again introduces some error. Considering the simulation bias caused by some parameters in the simulation that need to be estimated, the CFD-DEM model is reliable to study the fluid-solid flow characteristics of the proppant slurry in the fracture.

3.2. Effect of injection location

In fracturing, the location of the perforation is usually selected based on reservoir characteristics as well as the geomechanical properties of a formation in order to obtain better productivity. To study the effect of injection location on proppant placement, we simulated the supercritical CO_2 slurry injection at three different heights on the fracture inlet side. The distances from the center of the three injection clusters to the bottom are, respectively, 112.5 (top), 74.5 (middle), and 37.5 mm (bottom). In each case, the injection temperature is 338 K, the proppant density is 1250 kg/m^3, the injection proppant concentration is 0.04 and the injection time 20 s. Other parameters are shown in Table 1.

Fig. 3 shows a comparison of the proppant bank building process under the three injection locations. It is clear from the results shown in the figure that different perforation positions have a greater impact on the transport and placement of proppant. The top injection causes the proppant particles to settle in a relatively dispersed manner, resulting in a more uniform proppant bank distribution than middle and bottom injection. This is because the injected proppant slurry and the surrounding supercritical CO_2 fluid will generate a large number of vortices under the effect of viscous shear (Longmire and Eaton, 1992), and then form a swirling vortex. The motion of swirling vortex promotes the diffusion of proppant particles in the fracture. This phenomenon was also observed by Baldini et al. (2018) in their study of slickwater transport proppant. However, since the viscosity of supercritical CO_2 is considerably lower than that of slickwater, the particles are not carried by the swirling vortex to be dispersed above the injected stream in our simulation. Therefore, the swirling vortex that form beneath the injected beam influence the development of the proppant bank.
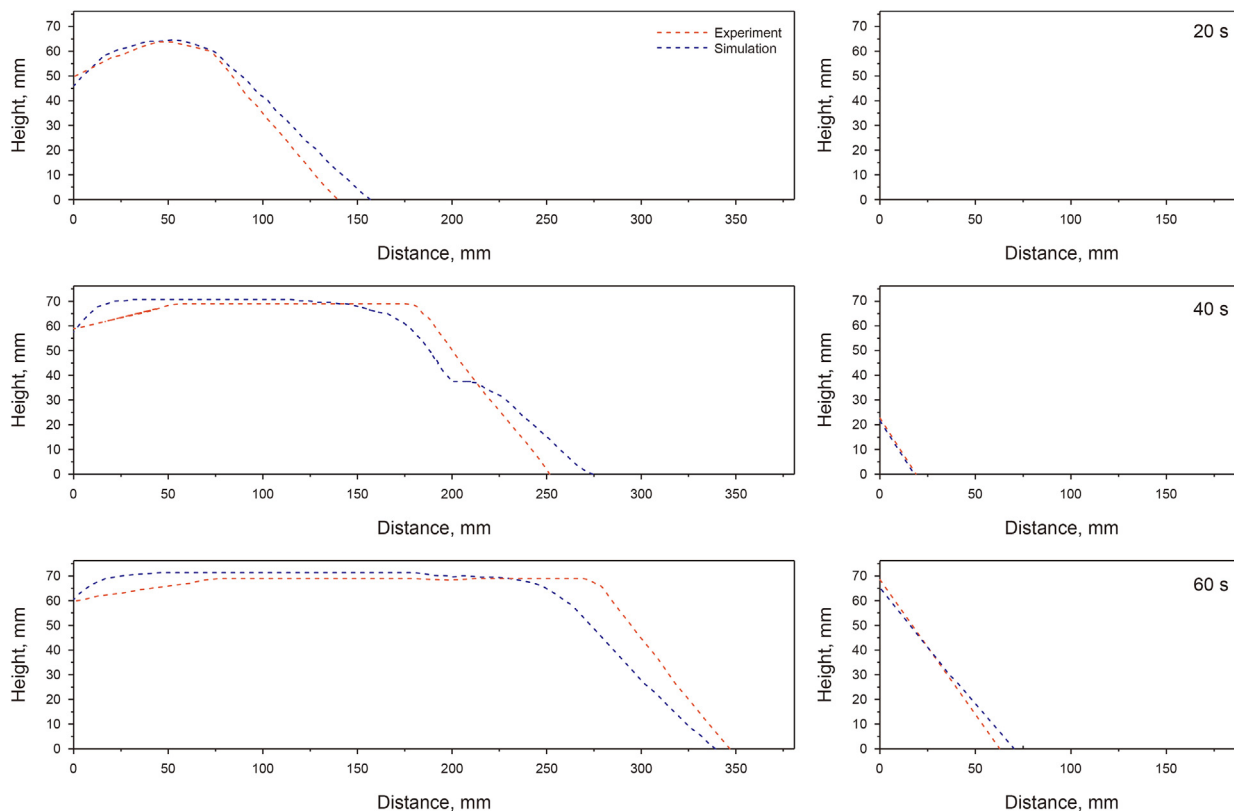
Fig. 2. Comparison of proppant bank profiles in the main fracture (left) and bypass fracture (right) in simulation result and experimental data.
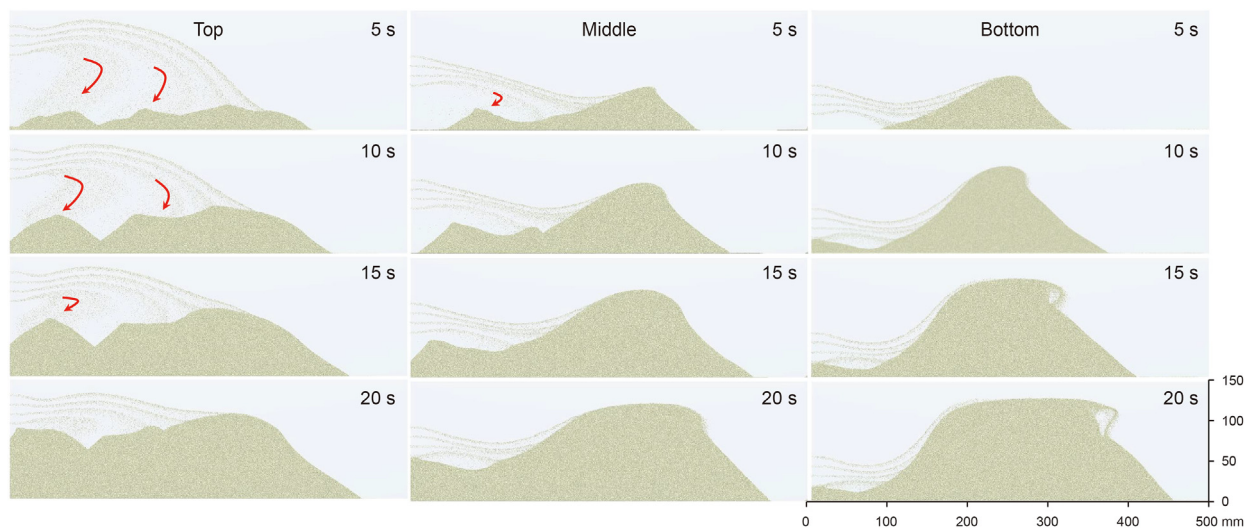
Fig. 3. The proppant placement process for different injection locations.
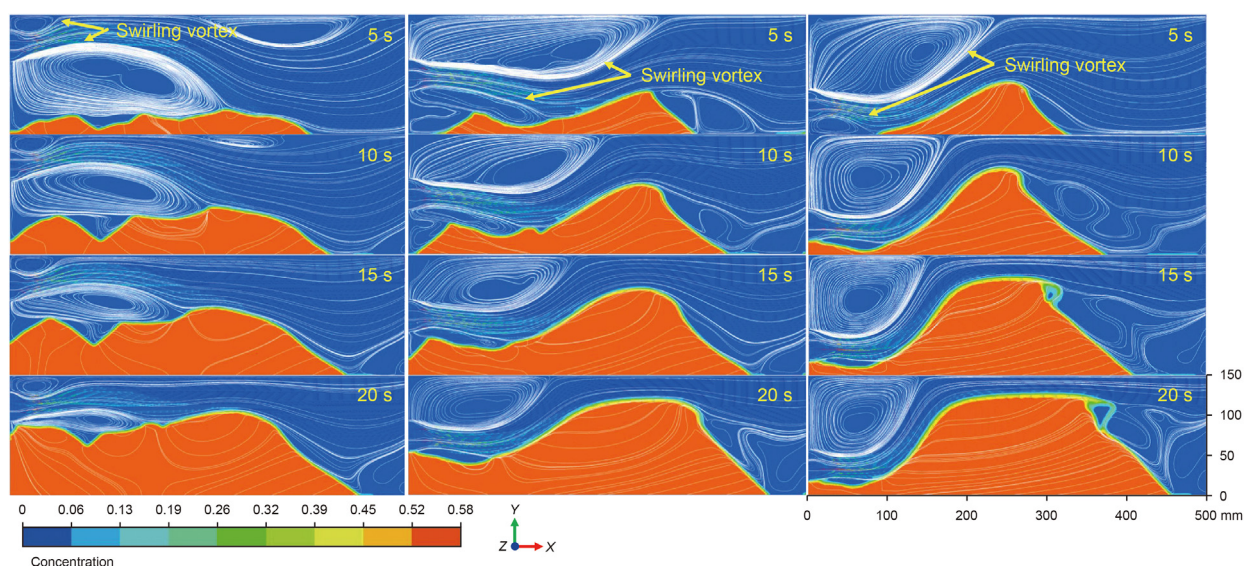

Fig. 4. The streamline of top injection (first column), middle injection (second column) and bottom injection (third column).

To clarify the distribution of swirling vortices in the fracture at the three injection positions, we have given the corresponding streamlines on the center plane of the fracture, as shown in Fig. 4. It can be observed that the swirling vortex is mainly below the injection point in the top injection (first column), while in the middle injection (second column) and bottom injection (third column) it is above the injection point. With time, the vortex area in the top injection decreases, and the vortex area in the middle and bottom injection tends to be constant. At the initial stage of the middle injection, there is a small swirling vortex under the slurry stream, and then it gradually disappears. However, the dispersion of the proppant particles within the fluid is also affected, resulting in the formation of relatively uniform proppant bank compared to bottom injection. In the bottom injection, due to the limitation of space below the injection point, the vortex is weak, and the proppant mainly moves along the dune surface by the erosion of the fluid. In addition, when the fluid reaches a certain velocity, a phenomenon of the proppant making a circular motion at the tail of the bank occurs.

In conclusion, the swirling vortex generated below the injection point when injecting supercritical CO_2 slurry can increase the diffusion of the proppant, which in turn leads to a more uniform spreading of the proppant bank near the wellbore. After the vortex below the injection point disappears as the proppant bank grows, the proppants are fluid-driven and spread deeper into the fracture along the bank surface. Therefore, top injection is an effective way to improve the placement of the proppant in the fracture.

Table 3
Design of pumping schedules.

Order	Stage	Proppant concentration	Pumping time, s
Order 1	Stage 1	0.02	10
	Stage 2	0.04	5.0
	Stage 3	0.06	3.5
	Stage 4	0.08	2.5
Order 2	Stage 1	0.08	2.5
	Stage 2	0.06	3.5
	Stage 3	0.04	5.0
	Stage 4	0.02	10

3.3. Effect of multi-concentration injection order

In this section, the placement of proppant under multi-concentration injection orders are investigated. Two different multi-concentration proppant injection orders are designed as shown Table 3. In order 1, the proppant concentration increases from stage 1 to stage 4. In order 2, the proppant concentration decreases from stage 1 to stage 4. The number of proppant particles injected in each stage of the two schemes is the same, so the total injection time of each stage is different. Other parameters are shown in Table 1, in which the injection temperature and proppant density are fixed at 338 K and 1250 kg/m^3, respectively.

Fig. 5 shows the fluid velocity contours and proppant placement in the fracture after each injection stage in different injection orders. It can be observed that the shape of the proppant bank in the fracture is basically similar in each stage of the two orders. Compared to order 1, proppant transport in stage 1 of order 2 show longer distance under the same injection velocity conditions, which induce more smoothly proppant distribution in the fracture. This is because the proppant particles in the slurry with high concentration have higher velocity in the direction of flow and a lower settling velocity in the vertical direction in the initial injection stage (Blyton et al., 2015). Furthermore, from the fluid velocity contours in the fracture illustrated in Fig. 5, we can observe that from stage 2 of the two injection orders, the proppant dunes gradually approached the high velocity flow region formed by supercritical CO$_2$ slurry injection, and the surface of the dunes began to be washed by the carrying fluid. This means that the shape of the proppant bank formed in the previous stage will also affect the proppant placement in the next stage by changing the distribution of the high-speed flow region.

To determine the effect of multi-concentration injection order on the proppant placement in the fracture, we present the final proppant bank profile of each stage and the *X*-direction component of fluid velocity in the moving layer of the dune surface along the centerline, as shown in Fig. 6. According to the coordinate system established in Fig. 1, the velocity component in the *X*-direction is the average velocity of the fluid in the horizontal flow direction on the centerline. It can be observed that order 2 has a clear advantage in the spread distance of proppant banks, which is 11.21% higher than that in order 1. Furthermore, Fig. 6 shows that there is a direct relationship between the proppant bank shape and the fluid velocity in the *X*-direction. For the fluid velocity in the *X*-direction, the flow to the fracture tip is positive, while flow to the wellbore is negative. The dashed line in the figure shows that there are two flow directions for the fluid near the surface of the proppant bank. In stage 1, the cutoff point for these two opposite directions of flow is approximately in the middle of the dune, and as the dune grows, the cutoff point in subsequent stages begins to move toward the wellbore.

At the same time, we can find from Fig. 6 that the fluid velocity in order 2 is higher than in order 1 in both stages 1 and 2, whether it is positive or negative. However, in stages 3 and 4, an inverse relationship displays: the fluid velocity in order 1 begins to be greater than in order 2. Combining the proppant concentration of the two injection orders in each stage, we can conclude that the velocity of the proppant bank surface fluid is proportional to the proppant injection concentration. Moreover, it can be also observed from Fig. 6 that after a cone-shaped dune appears in the fracture (starting from stage 2), increasing the proppant concentration mainly affects the fluid velocity near the dune front. In the final stage 4 of the simulation, although the fluid velocity on the dune front in order 1 is about twice as high as that in order 2 due to the high injection concentration, the bank spreading distance is still shorter. In fracturing operation, proppant concentration is mostly injected in the way of step increase, while this study shows that a longer proppant spreading distance may be obtained by using a step decrease concentration injection method under the premise of effectively avoiding sand plugging at the fracture entrance. Therefore, the proppant concentration combination should be reasonably selected in the pumping design to obtain a longer dune placement distance.
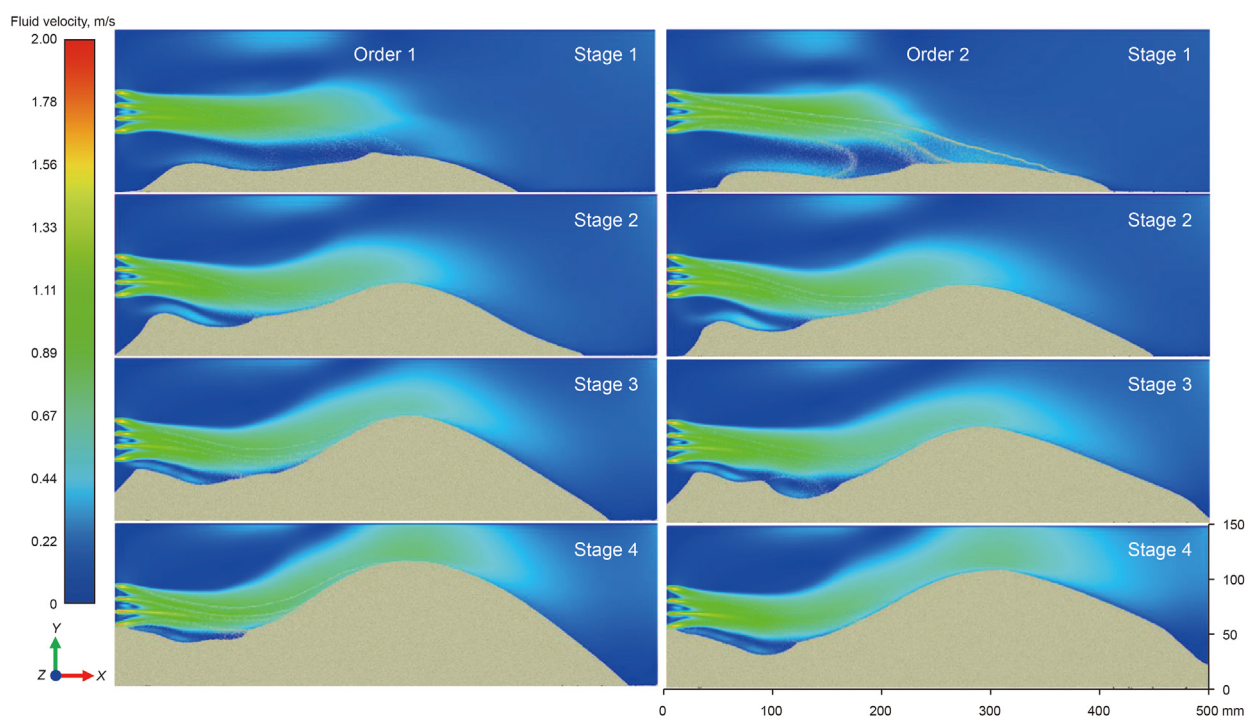

Fig. 5. Fluid velocity contours and proppant placement in the fracture after each injection stage.
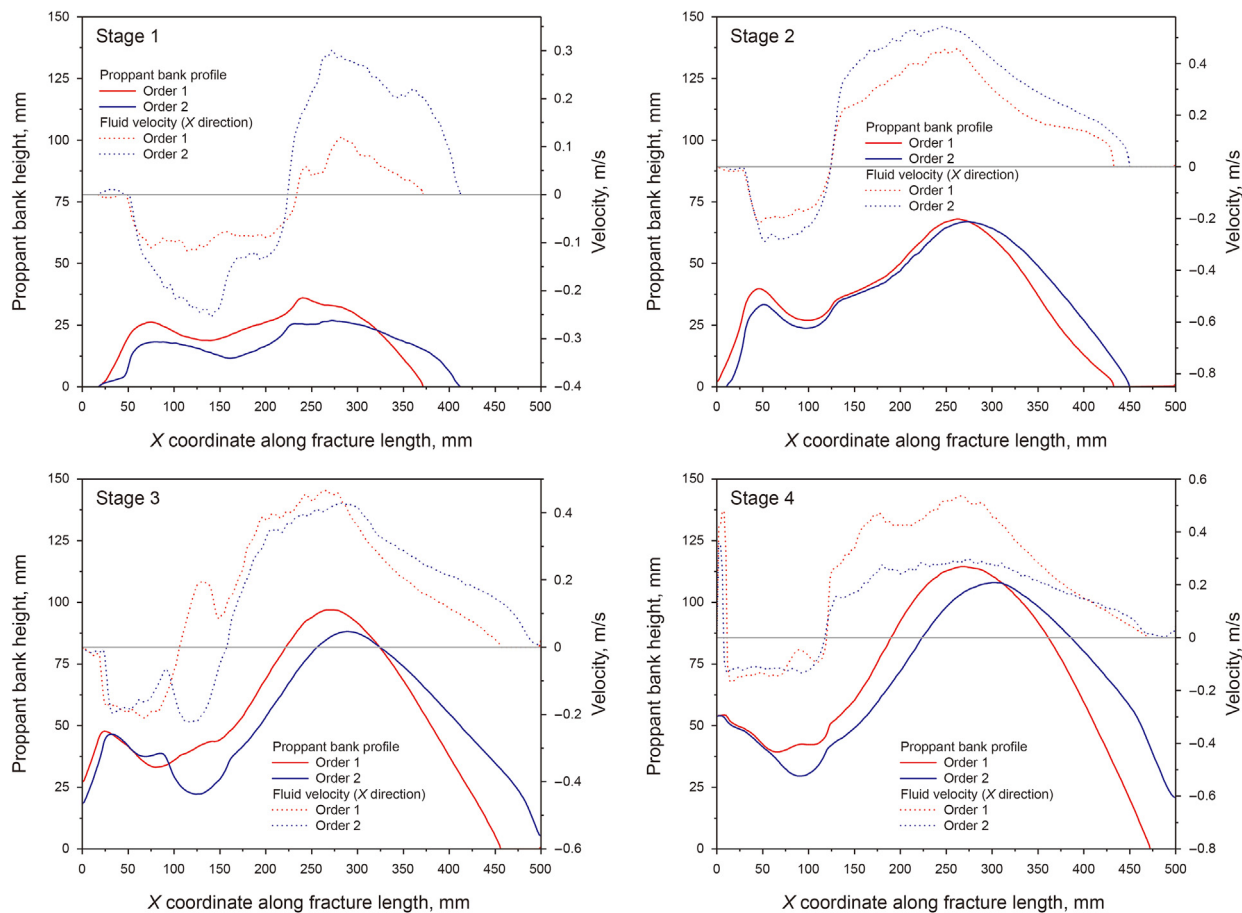
Fig. 6. Final proppant bank profile (solid line) of each stage and the *X*-direction component of fluid velocity in the moving layer of the dune surface along the centerline (dashed line).

3.4. Effect of multi-density injection order

For pumping slurry, the proppant with low density can reach the deeper fracture with the slurry, because its settling velocity in the fluid is decreased. However, the compressive strength of proppant also weaken with the decrease of density, which makes it easy to break when the fracture is closed, resulting in reduce of fracture conductivity. To investigate the effect of multi-density injection order on proppant placement, in this section we have designed two proppant pumping schedules with different injection orders as shown in Table 4. In order 1, the proppant density increases from stage 1 to stage 3. In order 2, the proppant density decreases from stage 1 to stage 3. Other parameters are shown in Table 1, in which the injection temperature and proppant concentration are fixed at 338 K and 0.04, respectively.

To illustrate the placement process of the proppant under multi-density injection order, we present the proppant bank distribution

Table 4
Design of pumping schedules.

Order	Stage	Proppant density, kg/m³	Pumping time, s
Order 1	Stage 1	1250	6
	Stage 2	2650	6
	Stage 3	3500	6
Order 2	Stage 1	3500	6
	Stage 2	2650	6
	Stage 3	1250	6

after each injection stage in Fig. 7. It is evident that proppants of different densities show significantly different distribution structures in the fracture under the two designed injection orders. For the proppant placement in order 1, the low-density proppant spreads a relatively uniform proppant bed at the bottom of the fracture in the initial stage. Then, the medium-density proppant injected in stage 2 basically settles and accumulates on the proppant bed formed in stage 1 and does not over the peak of this bed. Subsequently, the high-density proppant injected in stage 3 cover the highest point of the dunes in the previous two stages and travel deep into the fracture, but still does not exceed the laying distance of the low-density proppant bed. In order 2, the high-density proppant first injected forms a distinct dune near the injection points. Then, the medium density proppant injected in the secondary stage completely cover the proppant dune and maintain the similar shape as before. When the low-density proppant was injected in the third stage, most of the proppant was washed to the back side of the dune except a small part of them accumulated in the front side of the dune, which promoted the proppant to be spread deep into the fracture. Comparing the placement process of proppant bank under the two injection schedules, it can be seen that there is obvious scouring phenomenon of the proppant dune in the stage 3 of the injection order 2, which makes the proppant easier to migrate to the depth of the fracture.

Additionally, we also extracted the profiles of the proppant bank along the fracture length direction after the end of each injection stage in the two schedules, to determine the effect of the injection order of different density proppant on the proppant bank spread, as
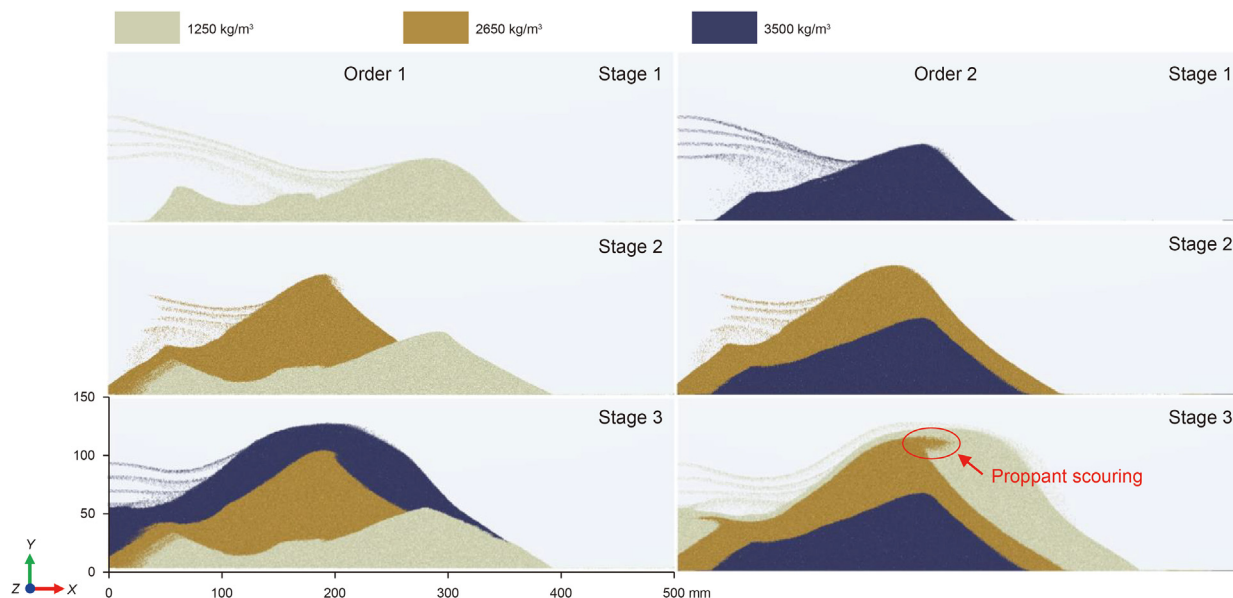
Fig. 7. The proppant bank distribution in the fracture after each injection stage.

shown in Fig. 8. It can be clearly seen from Fig. 8 that after the completion of the three injection stages in order 1, the placement distance of proppant in the fracture does not increase noticeably, which are 367, 391, and 392 mm, respectively, which increased by 4.08% compared with the laying distance in order 1. In order 2, the proppant bank placement distance between different injection stages increased greatly, and the spread distance are 297, 338, and 408 mm, respectively. The high-density proppant injected in order 1 can inhibit the scouring development to some extent by increasing the driving force of proppant particles needed, reduce the transport efficiency of the proppant. In contrast, the steep dune formed by the high-density proppant first injected in order 2 increased the velocity of the fluid flowing through it, enhancing the lifting effect on subsequent low-density proppant particles. Moreover, low-density proppant is more likely to be washed away when it is on top of the dune. Thereby, when pumping by multi-density injection, on the premise of avoiding premature accumulation of

proppant bank to block the entrance, injecting high-density proppant first can, to a certain extent, facilitate the transport of the low-density proppant injected later in the fracture.

3.5. Effect of injection temperature

In a typical fracturing operation, the temperature of the injected fluid is lower than that of the reservoir. As the fluid flows in the fractures, heat transfer occurs between the fracturing fluid and the formation rock, resulting in variations in the properties of supercritical CO_2. In this section, three sets of injection temperature, 328, 338, and 348 K are designed to investigate the effect of fluid temperature on proppant distribution under otherwise the same conditions. In each case, the proppant density and injection proppant concentration are 2650 kg/m^3 and 0.04, respectively. It is generally believed that viscosity is an important factor reflecting the proppant carrying capacity of the fluid. Fig. 9 shows the viscosity distribution of supercritical CO_2 fluid and proppant placement in the
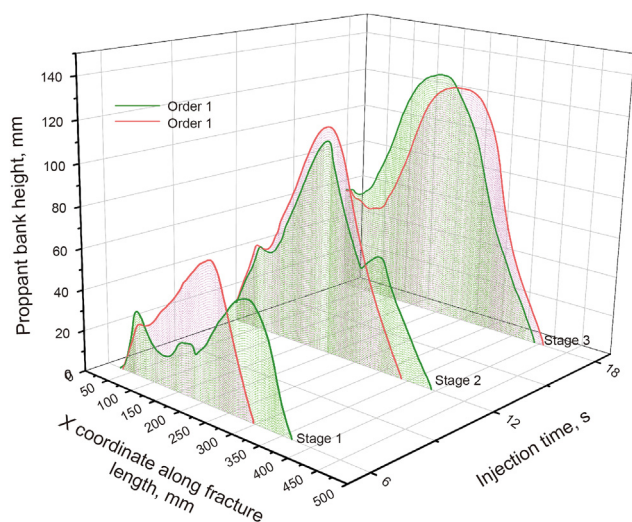

Fig. 8. The profiles of the proppant bank along the fracture length direction after the end of each stage in multi-density injection orders.
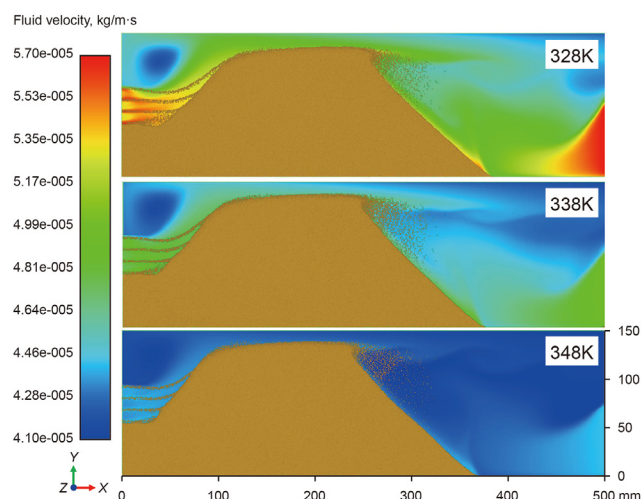

Fig. 9. Viscosity distribution and proppant placement of supercritical CO_2 fluid in fractures at different injection temperatures.
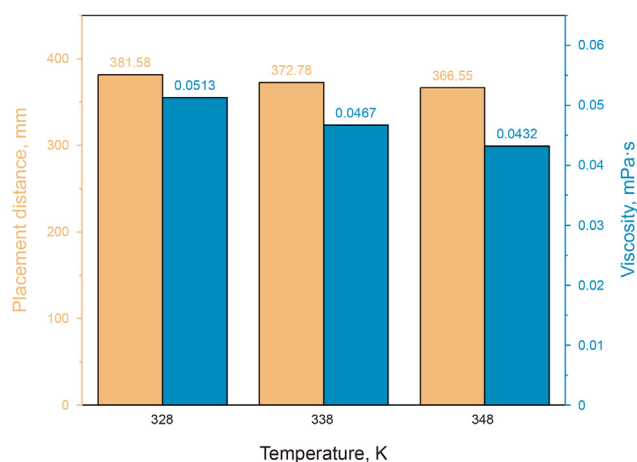
Fig. 10. Placement distance and the fluid viscosity of supercritical CO_2 at different injection temperatures.

fracture at different injection temperatures. It can be seen from the figure that for the same reservoir, the proppant slurry injection temperature will have a significant impact on the viscosity of supercritical CO_2 in the fracture. The viscosity of supercritical CO_2 depends on ambient temperature and pressure. With the same total injection time, outlet pressure and constant wall temperature, the temperature of supercritical CO_2 is directly related to the injection temperature when flowing in the fracture. Therefore, the viscosity of the fluid whose initial injection temperature is 328 K is higher than the other two temperatures in the fracture, which affects the placement of proppant.

To quantitatively compare the placement of the proppant in the three cases, the placement distance of proppant bank in the fracture and the fluid viscosity of supercritical CO_2 at different injection temperatures are given, as shown in Fig. 10. The fluid viscosity is the average value of supercritical CO_2 fluid at the fluidization layer on the proppant bank surface. It can be seen from the figure that as the temperature of the injected slurry decreases from 348 to 338 K and 328 K, the viscosity of the fluid carrying proppant particles increases by 8.1% and 18.75%, respectively. At the same time, the placement distance of proppant bank in the fracture also increases, increases by 1.70% and 4.10%, respectively. This shows that reducing the injected slurry temperature can improve the viscosity of supercritical CO_2 fluid, increase its driving force on proppant particles, enhance the carrying capacity, and obtain a longer proppant placement distance.

4. Conclusions

In the present paper, a coupled CFD-DEM method was adopted to study the proppant transport and placement in a planar fracture with perforation tunnel under different pumping schedule during supercritical CO_2 fracturing. The effects of several groups of different pumping schemes on the placement of the proppant is analyzed, which has some guiding significance for the design of the proppant pumping schedule. Main conclusions are drawn as follows:

(1) Different from conventional fracturing fluids, when supercritical CO_2 slurry is injected, it is the swirling vortex formed below the injection point that affects the diffusion of the proppant within the fracture, which in turn results in a more uniform distribution of proppant bank near the wellbore. The extent of the swirling vortex is positively correlated with the

injection height, thus supercritical CO_2 slurry injection in the upper part of the reservoir is an effective way to improve the distribution of the proppant in the fracture.

(2) For multi-concentration injection, the velocity of the fluid at the proppant bank surface is positively correlated with the concentration of the proppant injected. Under the conditions in this paper, a longer proppant bank placement distance is easily obtained with proppant injection concentration from high to low.

(3) During multi-density injection schedule, the high-density proppant injected first creates a prominent dune that will increase the velocity of the fluid as it flows through the dune, and the low-density proppant injected later is more easily carried deeper into the fracture by the fluid washout, creating a longer proppant bank.

(4) Proppant-carrying performance of supercritical CO_2 can be enhanced by decreasing the initial injection temperature. The lower initial temperature of supercritical CO_2 slurry contributes to obtain higher fluid viscosity, enhancing the driving effect of fluid on particles.

References

Alotaibi, M., Jennifer, M., 2019. Power law correlation for slickwater proppant dune height. In: SPE Hydraulic Fracturing Technology Conference and Exhibition, The Woodlands, Texas, USA. Society of Petroleum Engineers. https://doi.org/10.2118/194309-MS.

Alvarado, V., Manrique, E., 2010. Enhanced oil recovery: an update review. Energies 3 (9), 1529–1575. https://doi.org/10.3390/en3091529.

Bahrami, H., Rezaee, R., Clennell, B., 2012. Water blocking damage in hydraulically fractured tight sand gas reservoirs: an example from Perth Basin, Western Australia. J. Petrol. Sci. Eng. 88–89, 100–106. https://doi.org/10.1016/j.petrol.2012.04.002.

Baldini, M., Carlevaro, C.M., Pugnaloni, L.A., Sánchez, M., 2018. Numerical simulation of proppant transport in a planar fracture. A study of perforation placement and injection strategy. Int. J. Multiphas. Flow 109, 207–218. https://doi.org/10.1016/j.ijmultiphaseflow.2018.08.005.

Blyton, C.A.J., Gala, D.P., Sharma, M.M., 2015. A comprehensive study of proppant transport in a hydraulic fracture. SPE Annual Technical Conference and Exhibition. Society of Petroleum Engineers, Houston, Texas, USA. Society of Petroleum Engineers. https://doi.org/10.2118/174973-MS.

Chen, H., Hu, Y., Kang, Y., Wang, X., Liu, Y., 2021a. Advantages of supercritical CO_2 compound fracturing in shale on fracture geometry, complexity and width. J. Nat. Gas Sci. Eng. 104033. https://doi.org/10.1016/j.jngse.2021.104033.

Chen, H., Hu, Y., Liu, J., Liu, F., Wang, X., 2021b. Surface characteristics analysis of fractures induced by supercritical CO_2 and water through three-dimensional scanning and scanning electron icrography. J Rock Mech Geotech. https://doi.org/10.1016/j.jrmge.2021.04.006.

Clark, C.E., Horner, R.M., Harto, C.B., 2013. Life cycle water consumption for shale gas and conventional natural gas. Environ. Sci. Technol. 47 (20), 11829–11836. https://doi.org/10.1021/es4013855.

Cuéllar-Franca, R.M., Azapagic, A., 2015. Carbon capture, storage and utilisation technologies: a critical analysis and comparison of their life cycle environmental impacts. J CO_2 Util 9, 82–102. https://doi.org/10.1016/j.jcou.2014.12.001.

Dai, Z., Middleton, R., Viswanathan, H., Fessenden-Rahn, J., Bauman, J., Pawar, R., Lee, S.Y., McPherson, B., 2014. An integrated framework for optimizing CO_2 sequestration and enhanced oil recovery. Environ. Sci. Technol. Lett. 1 (1), 49–54. https://doi.org/10.1021/ez4001033.

Dehghanpour, H., Zubair, H.A., Chhabra, A., Ullah, A., 2012. Liquid intake of organic shales. Energy & Fuels 26 (9), 5750–5758. https://doi.org/10.1021/ef3009794.

Godec, M.L., 2011. Global Technology Roadmap for CCS in Industry. Sectoral Assessment CO_2 Enhanced Oil Recovery. Advanced Resources International, Arlington VA USA. https://www.unido.org/sites/default/fles/2011-05/EOR_0.pdf.

Gupta, Bobier, 1998. The history and success of liquid CO_2 and CO_2/N_2 fracturing system. SPE Gas Technology Symposium, Calgary, Alberta, Canada. Society of Petroleum Engineers. https://doi.org/10.2118/40016-MS.

Hamza, A., Hussein, I.A., Al-Marri, M.J., Mahmoud, M., Aparicio, S., 2021. CO_2 enhanced gas recovery and sequestration in depleted gas reservoirs: a review. J. Petrol. Sci. Eng. 196, 107685. https://doi.org/10.1016/j.petrol.2020.107685.

Heidaryan, E., Hatami, T., Rahimi, M., Moghadasi, J., 2011. Viscosity of pure carbon dioxide at supercritical region: measurement and correlation approach. J. Supercrit. Fluids 56 (2), 144–151. https://doi.org/10.1016/j.supflu.2010.12.006.

Holloway, S., 2005. Underground sequestration of carbon dioxide—a viable greenhouse gas mitigation option. Energy 30 (11–12), 2318–2333. https://doi.org/10.1016/j.energy.2003.10.023.

Huo, P., Zhang, D., Yang, Z., Li, W., Zhang, J., 2017. CO_2 geological sequestration: displacement behavior of shale gas methane by carbon dioxide injection. Int J Greenh Gas Con 66, 48–59. https://doi.org/10.1016/j.ijggc.2017.09.001.

Iddphonce, R., Wang, J., Zhao, L., 2020. Review of CO_2 injection techniques for enhanced shale gas recovery: prospect and challenges. J. Nat. Gas Sci. Eng. 77, 103240. https://doi.org/10.1016/j.jngse.2020.103240.

Jarrahian, A., Heidaryan, E., 2012. A novel correlation approach to estimate thermal conductivity of pure carbon dioxide in the supercritical region. J. Supercrit. Fluids 64, 39–45. https://doi.org/10.1016/j.supflu.2012.02.008.

Leung, D.Y.C., Caramanna, G., Maroto-Valer, M.M., 2014. An overview of current status of carbon dioxide capture and storage technologies. Renew. Sustain. Energy Rev. 39, 426–443. https://doi.org/10.1016/j.rser.2014.07.093.

Li, L., Zhao, N., Wei, W., Sun, Y., 2013. A review of research progress on CO_2 capture, storage, and utilization in Chinese Academy of Sciences. Fuel 108, 112–130. https://doi.org/10.1016/j.fuel.2011.08.022.

Li, X., Li, G., Yu, W., Wang, H., Zhang, S., 2018. Thermal effects of liquid/supercritical carbon dioxide arising from fluid expansion in fracturing. SPE J. 23 (6), 2026–2040. https://doi.org/10.2118/191357-PA.

Longmire, E.K., Eaton, J.K., 1992. Structure of a particle-laden round jet. J. Fluid Mech. 236, 217–257. https://doi.org/10.1017/S002211209200140X.

Meng, S., Yang, Q., Chen, S., Duan, Y., 2018. Fracturing with pure liquid CO_2: a case study. SPE Asia Pacific Oil and Gas Conference and Exhibition, Brisbane, Australia. Society of Petroleum Engineers. https://doi.org/10.15530/URTEC-2018-2918864.

Middleton, R.S., Carey, J.W., Currier, R.P., Hyman, J.D., Kang, Q., Karra, S., Jimenez-Martinez, J., Porter, M.L., Viswanathan, H.S., 2015. Shale gas and non-aqueous fracturing fluids: opportunities and challenges for supercritical CO_2. Appl. Energy 147, 500–509. https://doi.org/10.1016/j.apenergy.2015.03.023.

Middleton, R.S., Gupta, R., Hyman, J.D., Viswanathan, H.S., 2017. The shale gas revolution: barriers, sustainability, and emerging opportunities. Appl. Energy 199, 88–95. https://doi.org/10.1016/j.apenergy.2017.04.034.

Moghadam, A., Harris, N.B., Ayranci, K., Gomez, J.S., Angulo, N.A., Chalaturnyk, R., 2019. Brittleness in the devonian horn river shale, British Columbia, Canada. J. Nat. Gas Sci. Eng. 62, 247–258. https://doi.org/10.1016/j.jngse.2018.12.012.

Mojid, M.R., Negash, B.M., Abdulelah, H., Jufar, S.R., Adewumi, B.K., 2021. A state–of–art review on waterless gas shale fracturing technologies. J. Petrol. Sci. Eng. 196, 108048. https://doi.org/10.1016/j.petrol.2020.108048.

Naik, S., Yang, S., Woolley, M., Bedrikovetsky, P., 2019. Analytical modelling of the water block phenomenon in hydraulically fractured wells. J. Nat. Gas Sci. Eng. 67, 56–70. https://doi.org/10.1016/j.jngse.2019.04.018.

Norhasyima, R.S., Mahlia, T.M.I., 2018. Advances in CO_2 utilization technology: a patent landscape review. J CO_2 Util 26, 323–335. https://doi.org/10.1016/j.jcou.2018.05.022.

Patankar, S.V., 1980. Numerical Heat Transfer and Fluid Flow. Taylor & Francis. ISBN978-0-89116-522-4.

Qu, H., Tang, S., Liu, Z., Mclennan, J., Wang, R., 2021. Experimental investigation of proppant particles transport in a tortuous fracture. Powder Technol. 382, 95–106. https://doi.org/10.1016/j.powtec.2020.12.060.

Rightmire, C.M., Leshchyshyn, T.T., Vincent, M.C., 2005. The effects of proppant selection upon well productivity-a review of over 650 treatments in the Cardium formation. SPE Annual Technical Conference and Exhibition, Dallas, Texas. Society of Petroleum Engineers. https://doi.org/10.2118/96962-MS.

Roostaei, M., Nouri, A., Hosseini, S.A., Soroush, M., Fattahpour, V., 2020. A concise review of experimental works on proppant transport and slurry flow. SPE International Conference and Exhibition on Formation Damage Control, Lafayette, Louisiana, USA. Society of Petroleum Engineers. https://doi.org/10.2118/199310-MS.

Sahai, R., Moghanloo, R.G., 2019. Proppant transport in complex fracture networks – a review. J. Petrol. Sci. Eng. 182, 106199. https://doi.org/10.1016/j.petrol.2019.106199.

Song, X., Guo, Y., Zhang, J., Li, X., Li, X., 2019. Fracturing with carbon dioxide: from microscopic mechanism to reservoir application. Joule 3 (8), 1913–1926. https://doi.org/10.1016/j.joule.2019.05.004.

Span, R., Wagner, W., 1996. A new equation of state for carbon dioxide covering the fluid region from the triple-point temperature to 1100 K at pressures up to 800 MPa. J. Phys. Chem. Ref. Data 25 (6), 1509–1596. https://doi.org/10.1063/1.555991.

Sun, B., Wang, J., Wang, Z., Gao, Y., Xu, J., 2018. Calculation of proppant-carrying flow in supercritical carbon dioxide fracturing fluid. J. Petrol. Sci. Eng. 166, 420–432. https://doi.org/10.1016/j.petrol.2018.03.051.

Tong, S., Mohanty, K.K., 2016. Proppant transport study in fractures with intersections. Fuel 181, 463–477. https://doi.org/10.1016/j.fuel.2016.04.144.

Vengosh, A., Jackson, R.B., Warner, N., Darrah, T.H., Kondash, A., 2014. A critical review of the risks to water resources from unconventional shale gas development and hydraulic fracturing in the United States. Environ. Sci. Technol. 48 (15), 8334–8348. https://doi.org/10.1021/es405118y.

Wang, H., Li, G., Shen, Z., He, Z., Liu, Q., Zhu, B., Wang, Y., Wang, M., 2019. Expulsive force in the development of CO_2 sequestration: application of SC-CO_2 jet in oil and gas extraction. Front. Energy 13 (1). https://doi.org/10.1007/s11708-017-0458-6.

Wang, H., Li, G., Shen, Z., 2012. A feasibility analysis on shale gas exploitation with supercritical carbon dioxide. Energy Sources, Part A Recovery, Util. Environ. Eff. 34 (15), 1426–1435. https://doi.org/10.1080/15567036.2010.529570.

Wang, H., Li, G., Zheng, Y., Kamy, S., Shen, Z., Yang, B., Shi, L., 2020. Research status and prospects of supercritical CO_2 fracturing technology. Acta Pet. Sin. 41 (1), 116–126. https://doi.org/10.7623/syxb202001011.

Wang, H., Wang, M., Yang, B., Lu, Q., Zheng, Y., Zhao, H., 2018. Numerical study of supercritical CO_2 and proppant transport in different geometrical fractures. Greenhouse Gases: Sci. Technol. 8 (5), 898–910. https://doi.org/10.1002/ghg.1803.

Wang, J., Elsworth, D., 2020. Fracture penetration and proppant transport in gas- and foam-fracturing. J. Nat. Gas Sci. Eng. 77, 103269. https://doi.org/10.1016/j.jngse.2020.103269.

Wang, T., Tian, S., Li, G., Zhang, L., Ren, W., 2021. Molecular simulation of gas adsorption in shale nanopores: a critical review. Renew. Sustain. Energy Rev. 149, 111391. https://doi.org/10.1016/j.rser.2021.111391.

Yang, B., Wang, H., Wang, B., Shen, Z., Zheng, Y., Jia, Z., Yan, W., 2021. Digital quantification of fracture in full-scale rock using micro-CT images: a fracturing experiment with N_2 and CO_2. J. Petrol. Sci. Eng. 196, 107682. https://doi.org/10.1016/j.petrol.2020.107682.

Zheng, Y., Wang, H., Yang, B., Hu, Y., Shen, Z., Wen, H., Yan, W., 2020. CFD-DEM simulation of proppant transport by supercritical CO_2 in a vertical planar fracture. J. Nat. Gas Sci. Eng. 84, 103647. https://doi.org/10.1016/j.jngse.2020.103647.